Detailed chemical equilibrium model for porous ablative materials

J. Lachaud[a,*], Tom van Eekelen[b], James B. Scoggins, Thierry E. Magin[c], Nagi N. Mansour[d]

[a] *University of California Santa Cruz, Silicon Valley Initiatives, Moffett Field, California, USA*
[b] *Samtech, a Siemens company, Liège, Belgium*
[c] *von Karman Institute, Rhode-Saint-Genèse, Belgium*
[d] *NASA Ames Research Center, Moffett Field, California, USA*

Abstract

Ablative materials are used in thermal protection systems for atmospheric re-entry vehicle heat shields. A detailed chemical equilibrium heat and mass transport model for porous ablators is presented for the first time. The governing equations are volume-averaged forms of the conservation equations for gas density, gas elements, solid mass, gas momentum, and total energy. The element (gas) fluxes are coupled at the surface of the material with an inlet/outlet boundary condition, allowing modeling either atmospheric gases entering the porous material by forced convection or pyrolysis gases exiting the material. The model is implemented in the Porous material Analysis Toolbox based on OpenFOAM (PATO). The thermodynamics and chemistry library Mutation++ is used as a third party library to compute equilibrium compositions, gas properties, and solve the state-of-the-art boundary layer approximation to provide the ablation rate and the element mass fractions at the surface of the material. The model is applied to the detailed analysis of boundary layer and pyrolysis gas flows within a porous carbon/phenolic ablator characterized in a state-of-the-art arc-jet test. The selected configuration consists of an iso-flux ellipsoid-cylinder sample submitted to a $2.5\,MW/m^2$ heat flux with a decreasing pressure gradient from the stagnation point to the cylinder's side. During the first tenths of a second of the test, boundary layer gases percolate through the sample. Then, as the sample heats up, the

∗. Corresponding author : jean.lachaud@gadz.org

internal pressure increases inside the sample due to pyrolysis-gas production. The resulting pressure gradient blocks the boundary layer gases and leads to a pyrolysis gas flow that separates into two streams : one going towards the upper surface, and one going towards the lower pressure side under the shoulder of the sample. We show that the temperature profile is modified when using the detailed mass transport model. The sample's sub-shoulder zone is significantly cooled down while a temperature increase is observed in-depth. Implementing the model of this study in space agency codes will allow improving ground-test analyses and help provide more accurate material properties for design.

Keywords:
Porous media, equilibrium chemistry, ablation, pyrolysis, atmospheric entry

---

Nomenclature

A_j	Arrhenius law pre-exponential factor, SI
C_H	Stanton number for heat transfer
C_M	Stanton number for mass transfer
c_p	Specific heat, $J \cdot kg^{-1} \cdot K^{-1}$
e	Specific energy, $J \cdot kg^{-1}$
E_j	Arrhenius law activation energy, $J \cdot mol^{-1}$
F_j	Fraction of mass lost through pyrolysis reaction j
Fo	Forchheimer number
h	Specific enthalpy, $J \cdot kg^{-1}$
j	Diffusive flux, $mol \cdot m^{-2} \cdot s^{-1}$
K_i	Chemical equilibrium constant for reaction i
l	Thickness or length, m
m_j	Arrhenius law parameter
N_g	Number of gaseous species
n_j	Arrhenius law parameter

N_p	Number of pyrolysis reactions
p	Pressure, Pa
q	Heat flux, $J \cdot m^{-2} \cdot s^{-1}$
R	Perfect gas constant, $J \cdot mol^{-1} \cdot K^{-1}$
z	Mass fraction of the elements
Z_i	Gaseous element i
β	Klinkenberg coefficient, Pa
ϵ	Volume fraction
μ	Viscosity, $Pa \cdot s$
Π	Pyrolysis gas production rate, $kg \cdot m^{-3} \cdot s^{-1}$
ρ	Density, $kg \cdot m^{-3}$
τ	Characteristic time, s
ξ_j	Advancement of pyrolysis reaction j
ζ_{ji}	Mass-fraction production of element i in reaction j
a	Ablative material (gas, fiber, and matrix)
c	Char
e	Boundary layer edge properties
f	Fiber, fibrous preform
g	Gas phase
m, PM	Polymer matrix
mv	Virgin polymer matrix
p	Pyrolysis
pg	Pyrolysis gas
$\mathcal{F}_i$	Diffusion flux of the i^{th} element, $kg \cdot m^{-2} \cdot s^{-1}$
$\dot{m}$	Mass flow rate, $kg \cdot m^{-2} \cdot s^{-1}$
$\underline{\underline{\mathbf{K}}}$	Permeability tensor, s^2
$\underline{\underline{\mathbf{k}}}$	Conductivity tensor, $J \cdot m^{-2} \cdot s^{-1}$
$\mathbf{v}$	Convection velocity, $m \cdot s^{-1}$

1. Introduction

Space exploration missions often include entering a planet atmosphere at hypersonic speed. A high enthalpy hypersonic shock forms around the spacecraft and kinetic energy is progressively dissipated into heat [1]. Heat is transferred to the surface of the spacecraft by radiation and convection. A suitable heat shield is needed to protect the payload. The level of heat flux increases with entry speed and atmosphere density. For moderate speed entry, typically below $7.5\,km/s$, and mild heat fluxes, up to $1\,MW/m^2$, reusable materials are an adequate solution. A famed example is the ceramic tile used on the Space Shuttle Orbiter. For entry speeds higher than $8km/s$, heat fluxes exceeding $1.5\,MW/m^2$, and entry into high-density atmospheres imposes the use of ablative materials for Thermal Protection Systems (TPS). These mitigate the incoming heat through phase changes, chemical reactions, and material removal [2].

A critical problem in the design of ablative TPS is the choice of a heat shield material and its associated material response model. In the past, dense carbon/carbon and carbon/resin composites have been widely used for many ablative applications [2, 3], including space exploration [4]. The last decade has seen a renewed effort by scientists and engineers toward the development of a new class of carbon/phenolic (C/P) ablators specifically designed for high altitude breaking in Earth and Mars atmospheres. This new class of C/P composites is made of a carbon fiber preform partially impregnated with a low-density phenolic resin (Figure 1). They are very light with an overall density around $200kg/m^3$, are good insulators, and display sufficient mechanical properties for atmospheric reentry. A successful example is the phenolic-impregnated carbon ablator (PICA) developed at the NASA Ames Research Center [5] and flight qualified during the recent reentry missions of Stardust (Earth reentry at $12.7\,km/s$) [6] and the Mars Science Laboratory (Mars entry at $5.5\,km/s$) [7, 8]. This innovative development has been followed by the Space Exploration Technologies Corp. (SpaceX) with PICA-X , used on the commercial Dragon capsule, [1] and by Airbus Defense and Space with ASTERM, selected by the European Space Agency for future missions [9].

During atmospheric entry, low-density carbon/phenolic ablative materials undergo thermal degradation and ultimately recession captured by the

1. http ://www.spacex.com/news/2013/04/04/pica-heat-shield, retrieve Jan 1, 2014.

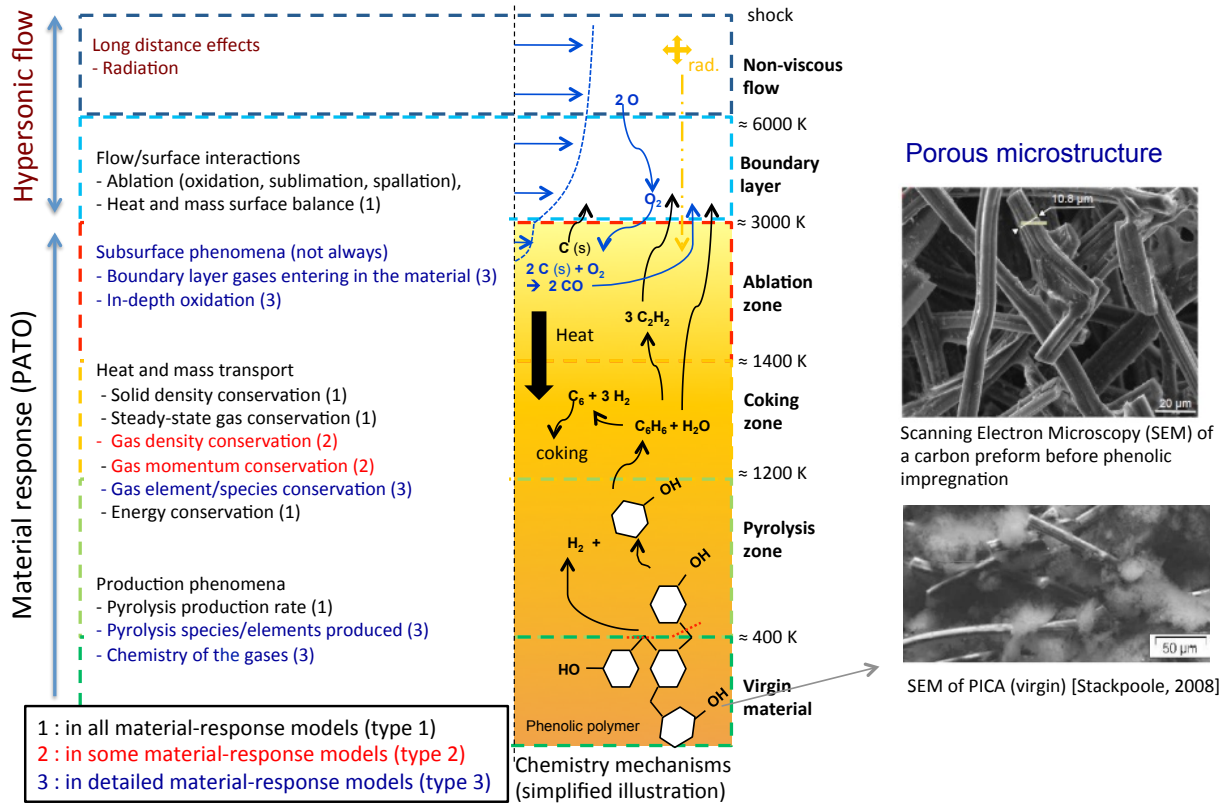

FIGURE 1: Phenomenology of porous carbon/phenolic ablative materials and levels of modeling

following physico-chemical phenomena (Figure 1) :

- Solid Pyrolysis (pyrolysis zone). Zone where the phenolic polymer thermally decomposes and progressively carbonizes into a low density carbon form, losing mass while releasing pyrolysis gases - hydrogen and phenol are shown as examples in Figure 1.
- Pyrolysis-gas Transport and Chemistry (char layer = coking zone and ablation zone). Zone where the pyrolysis gases released by solid pyrolysis percolate and diffuse to the surface through the network of pores. Reactions within the pyrolysis-gas mixture (homogeneous reactions) and between pyrolysis gases and the char take place with possible co-

king effects (heterogeneous reactions). Mixing and reaction of the pyrolysis gases with boundary layer gases into the pores of the material occur when boundary layer gases penetrate in the material by forced convection or due to fast diffusion at low pressures.

– Ablation Chemistry (ablation zone). Zone where after charring (and possible coking), the material is removed by ablation and the outer surface recedes. Depending on entry conditions, ablation may be caused by heterogeneous chemical reactions (oxidation, nitridation), phase change (sublimation), and possibly mechanical erosion (often called spallation). For porous materials, the thickness of the ablation zone depends on the thermo-chemical conditions and the material microstructure [10]. When the oxidation rate is slow and the diffusion rate is high, oxygen diffuses in the material and the oxidation zone extends to the bottom of the zone. During the end of the entry of Stardust, the ablation zone extends down to the pyrolysis zone [10]. At high temperatures, the surface of the material is in equilibrium chemistry conditions with the surrounding gas, all the oxygen is consumed at the surface of the ablator, and no in-depth ablation is observed. In the present study, we will study this latter regime.

Simplified models that possess analytical solutions in steady state [11] or when studying only a few of the coupled phenomena cited above [12, 13] are useful to bring a comprehensive understanding of a given aspect of the multi-physics phenomena. For design, the implementation of complete time-accurate models in numerical simulation tools is necessary.

A review of the open literature has revealed three levels of models used in twenty-five numerical simulation tools [14]. The first level (1), based on the state-of-the-art Charring Material Ablation [15] model, initially developed for dense ablators in the 1960s, is implemented in all design codes. The core phenomena of the pyrolysis/ablation problem are modeled but many simplifications are used. A major simplification is that the momentum-conservation is not implemented, meaning that the direction of the pyrolysis gas flow and the internal pressure need to be arbitrarily prescribed by the user. This type (1) model is well adapted for unidimensional, quasi steady-state, and equilibrium chemistry conditions with constant element fractions. Type (1) models [15, 16, 17] have enabled successful porous heat-shield design but have required the use of large safety margins to compensate for possible prediction errors [7]. However, post flight analyses of MSL flight data have shown that type (1) material models provide inaccurate flight predictions

when using ground data [8]. The second level (2) of modeling includes the implementation of the momentum conservation. This capability is found in a few design codes and in several recent analysis codes allowing the determination of gas flow directions for constant element/species mixtures. Type (3) models include element and/or species conservation equations, and associated equilibrium and/or finite-rate chemistry models, for a more rigorous modeling of heat and mass transport phenomena. No detailed type (3) model using the equilibrium chemistry assumption has been proposed yet. The principal objective of this article is to present a rigorous type 3 model using the equilibrium chemistry assumption. The second objective is to apply it to the analysis of a state-of-the-art ground test.

Extensive ground test campaigns are carried out to test and qualify new materials before flight [17]. Ground test data are used to develop the material response models needed for heat-shield design. Plasma arc-jet tests that can simulate on the ground a wide range of extreme conditions, often directly representative of flight conditions, are on the critical path of material qualification and model development. For the development of nominal material-response models, it is necessary to design tests with well controlled heat loads - as homogeneous as possible and constant in time. Hemisphere-cylinder samples are used - with the hemispheric side facing the flow. They display the remarkable advantages of featuring an almost constant flux (also, called iso-flux or Iso-Q) over most of the front face, both in space and in time. Also, they tend to preserve their shape as they ablate. Modeling the in-depth thermal response of Iso-Q samples is still far from trivial. It has been shown that to model correctly the conductive heat transfer, a two dimensional axisymmetrical code is required [17]. The pressure profile over the outer surface is almost constant over the hemisphere but strongly decreases after the shoulder, such that strong pressure gradients and complex gas flow features occur. In some cases, boundary layer gases may be forced to pass through the sample. These effects strongly affect the overall heat transport. The type 3 equilibrium model will be applied to the analysis of the multi-dimensional gas flow and the resulting heat transport modifications. Three model hypotheses will be compared : 1) boundary layer gases are not allowed to enter the porous material (state-of-the art technique [17, 18]), 2) a fictitious flow of pyrolysis gases is allowed to enter the sample instead of the boundary layer gases (option available in more advanced ablation codes [19, 20]), 3) boundary layer gases are allowed to enter the sample (option only available in the upgraded version of the code used for the present study). The expected

output of this work is a better understanding of gas-flow and heat transport by the gases in porous materials during arc-jet testing. It will enable a better estimation of material properties and help reducing design uncertainties.

2. Model

The detailed *type-3* equilibrium ablation model presented in this section is based on a volume-averaged [21] mathematical framework adapted for porous ablative materials [20]. The mathematical framework proposed is fully compatible with ablative material models based on the Charring Material Ablation (CMA) reference model [14] while allowing for the inclusion of additional physics-based phenomena. In this section, the governing equations and the boundary conditions are presented.

2.1. Governing equations

The governing conservation equations for mass, species, momentum, and energy-conservation are summarized in the following subsections.

2.1.1. Mass-conservation equations : gas, species/elements, solid

The gaseous mass conservation equation includes a production term (right-hand side) to account for the pyrolysis gas production, noted Π, and reads

$$\partial_t(\epsilon_g \rho_g) + \partial_{\mathbf{x}} \cdot (\epsilon_g \rho_g \mathbf{v_g}) = \Pi \tag{1}$$

The pyrolysis gas production - Π - is traditionally obtained by fitting thermogravimetry analysis of the resin decomposition using one or several Arrhenius laws [22]. A convenient notation for $j \in [1, N_p]$ pyrolysis reactions is

$$PM_j \rightarrow \sum_{i=1}^{N_g} \zeta_{ji} Z_i \tag{2}$$

where PM_j is a fictitious solid species of the pyrolyzing polymer matrix (PM) and ζ_{ji} is the mass fraction production of element Z_i in reaction j. The pyrolyzing matrix density is then given by

$$\epsilon_m \rho_m = \epsilon_{mv} \rho_{mv} \sum_{j=1}^{N_p} F_j (1 - \xi_j) \tag{3}$$

where

$$\frac{\partial_t \xi_j}{(1-\xi_j)^{m_j}} = T^{n_j} \mathcal{A}_j \exp\left(-\frac{E_j}{\mathcal{R}T}\right) \tag{4}$$

The element production is given by

$$\pi_i = \epsilon_{mv} \rho_{mv} \sum_{j=1}^{N_p} F_j \zeta_{ji} \partial_t(\xi_j) \tag{5}$$

and the overall pyrolysis-gas production is obtained by summing over i and reads

$$\Pi = \epsilon_{mv} \rho_{mv} \sum_{j=1}^{N_p} F_j \partial_t(\xi_j) \tag{6}$$

Past models and studies have considered a constant element fraction of the pyrolysis gases [14]. The conservation equations for the element mass fractions are needed to accurately track element transport within the pores of the material (allowing for possible penetration of air in the material). The conservation equations for the element mass fraction (z_i) reads

$$\partial_t(\epsilon_g \rho_g z_i) + \partial_{\mathbf{x}} \cdot (\epsilon_g \rho_g z_i \mathbf{v_g}) + \partial_{\mathbf{x}} \cdot \mathcal{F}_i = \pi_i \tag{7}$$

where, $\mathcal{F}_i$ is the diffusion flux of the i^{th} element.

The volume-averaged density change of the matrix due to pyrolysis -Π - is modeled using

$$\partial_t(\epsilon_m \rho_m) = -\Pi \tag{8}$$

2.1.2. Momentum conservation in porous media

The gas velocity is obtained by resolution of the momentum-conservation equation. In this study, we consider creeping (Stokes) flows in the continuum regime in the pores of the material. Under this hypothesis, the averaged momentum conservation takes the form of Darcy's law [23]. It may be written as

$$\mathbf{v_g} = -\frac{1}{\epsilon_g \mu} \underline{\underline{\mathbf{K}}} \cdot \partial_{\mathbf{x}} p \tag{9}$$

Most of the real porous materials are anisotropic, therefore, the permeability - $\underline{\underline{\mathbf{K}}}$ - is a second order tensor.

2.1.3. Energy conservation

According to Puiroux et al. [24], solid and gas phases are in thermal equilibrium as long as the Péclet number for diffusion of heat within the pores is small ($Pe = \epsilon_g \rho_g c_{p,g} d_p v_g / k_g$). For the space applications using low density carbon/phenolic ablators, the small pore size ($< 100\mu m$) [10] and the relatively slow pyrolysis gas flow ($v_g \sim 1m/s$) insure a small Péclet number : the gas temperature equilibrates to the solid temperature within the pores. Under the thermal equilibrium assumption, the energy conservation may be written as

$$\partial_t(\rho_a e_a) + \partial_{\mathbf{x}} \cdot (\epsilon_g \rho_g h_g \mathbf{v_g}) + \partial_{\mathbf{x}} \cdot \sum_{i=1}^{N_g} (h_i \mathcal{F}_i) = \partial_{\mathbf{x}} \cdot (\underline{\underline{\mathbf{k}}} \cdot \partial_{\mathbf{x}} T) + \mu \epsilon_g^2 (\underline{\underline{\mathbf{K}}}^{-1} \cdot \mathbf{v_g}) \cdot \mathbf{v_g} \quad (10)$$

where the total (storage) energy of the ablative material is the sum of the energy of its components

$$\rho_a e_a = \epsilon_g \rho_g e_g + \epsilon_m \rho_m h_m + \epsilon_f \rho_f h_f \quad (11)$$

and the second and third terms of the left-hand side are the energy convected (advection) and the energy transferred (diffusion) by the pyrolysis gases, respectively. Heat transfer is conveniently modeled as an effective diffusive transfer (Fourier's law). The effective conductivity - $\underline{\underline{\mathbf{k}}}$ - is a second order tensor accounting for conduction in the solid, conduction in the gas, and effective radiative heat transfer. The second term on the right-hand side is the energy dissipated by viscous effects in Darcian regime [23].

Conductivity is the main mode of heat transfer. To solve implicitly Eq. 10, it is therefore convenient to develop it and express it in terms of temperature. The first term reads

$$\partial_t(\rho_a e_a) = \partial_t(\epsilon_g \rho_g e_g) + \partial_t(\epsilon_m \rho_m h_m) + \partial_t(\epsilon_f \rho_f h_f) \quad (12)$$

$$= \partial_t(\epsilon_g \rho_g (h_g - p/\rho_g)) + \epsilon_m \rho_m c_{p,m} \partial_t T + h_m \partial_t(\epsilon_m \rho_m) + \epsilon_f \rho_f c_{p,f} \partial_t T + h_f \partial_t(\epsilon_f \rho_f) \quad (13)$$

Eq. 10 is then rearranged as follows

$$(\epsilon_m \rho_m c_{p,m} + \epsilon_f \rho_f c_{p,f}) \, \partial_t T - \partial_{\mathbf{x}} \cdot (\underline{\underline{\mathbf{k}}} \cdot \partial_{\mathbf{x}} T) = \left| \begin{array}{l} -h_m \partial_t(\epsilon_m \rho_m) - h_f \partial_t(\epsilon_f \rho_f) \\ -\partial_t(\epsilon_g \rho_g h_g - \epsilon_g p) + \partial_{\mathbf{x}} \cdot (\epsilon_g \rho_g h_g \mathbf{v_g}) \\ +\partial_{\mathbf{x}} \cdot \sum_{i=1}^{N_g} (h_i \mathcal{F}_i) + \mu \epsilon_g^2 (\underline{\underline{\mathbf{K}}}^{-1} \cdot \mathbf{v_g}) \cdot \mathbf{v_g} \end{array} \right. \quad (14)$$

and implicitly solved in temperature.

Experimentally, composite material properties are more conveniently measured in mixed fiber-and-matrix virgin (v) and char (c) states. The enthalpy of the matrix (h_m) - which is the only decomposing phase in the present study - is historically noted $\bar{h}$ [25], and reads

$$h_m = \bar{h} = \frac{\rho_v h_v - \rho_c h_c}{\rho_v - \rho_c} \tag{15}$$

The term $\partial_t(\epsilon_f \rho_f)$ accounts for possible in depth ablation or coking. In depth heterogeneous phenomena are slow processes [26, 27] that are neglected in state-of-the-art models [17]. In this study, we will also assume that no heterogeneous chemistry occurs in depth.

2.2. Boundary conditions

At the bottom of the Iso-Q sample, conservative boundary conditions are used (adiabatic and impermeable). At the wall, a convective boundary condition is used. The surface energy balance and the surface mass balance are resolved to compute the heat load, and the mass flow at the surface.

2.2.1. Surface energy balance

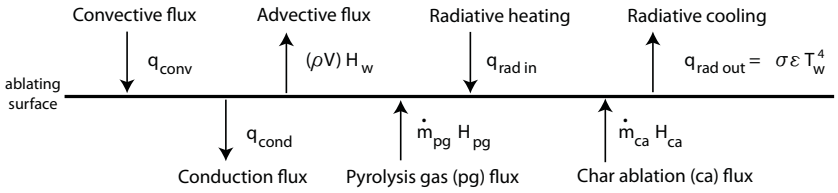

FIGURE 2: Energy balance at the wall

The surface energy balance at the wall depicted in Fig. 2 reads

$$q_{conv} - (\rho V)h_w + q_{rad,in} - q_{rad,out} - q_{cond} + \dot{m}_{pg}h_{pg} + \dot{m}_{ca}h_{ca} = 0 \tag{16}$$

where the convective heat flux - $q_{conv} = \rho_e u_e C'_H (h_e - h_w)$ - and the radiative heat flux are extracted from CFD simulations. The Stanton number C_H is corrected to account for the blockage induced by the pyrolysis/ablation gas blowing ; that is, the heat transfer coefficient is corrected. For example, the

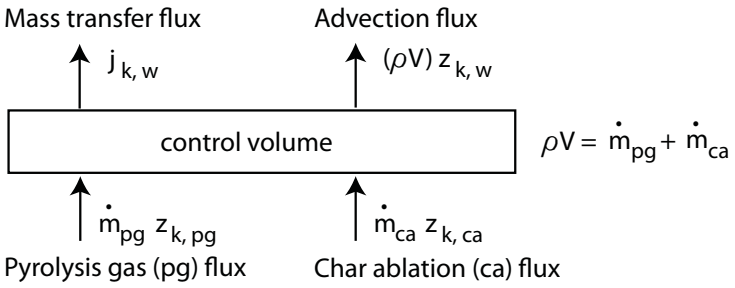

FIGURE 3: Element mass-fraction conservation at the wall

following correction is widely used $C'_H = C_H\, ln(1 + 2\lambda B')/ln(2\lambda B')$, where $B' = (\dot{m}_{pg} + \dot{m}_{ca})/(\rho_e u_e C_M)$ is a dimensionless mass flow rate and λ is a scaling factor usually taken equal to 0.5 [28]. The resolution of Eq. 16 requires the evaluation of the pyrolysis-gas flow rate - $\dot{m}_{pg}$ - and of the ablation rate - $\dot{m}_{ca}$.

2.2.2. Surface mass balance and recession rate

The pyrolysis-gas flow rate - $\dot{m}_{pg}$ - is directly obtained in the material-response code by integration of the pyrolysis, transport, and mass equations, as explained previously. However, the ablation rate - $\dot{m}_{ca}$ - is a function of both the mass transfer in the boundary layer and the thermo-chemical properties at the wall (pyrolysis-gas blowing rate and composition, temperature, pressure, boundary-layer gas composition). A common practice is to assume thermochemical equilibrium at the wall to compute the ablation rate. The model still in use in the community was developed in the sixties [29]. It is based on element conservation in steady-state in a control volume close to the wall as sketched in Fig. 3 and expressed in Eq. 17. The underlying hypothesis is that over a time increment Δt (corresponding to the numerical time step in the material response code), the equilibrium chemistry problem in the control volume is quasi-steady (p, T, $\dot{m}_{pg}$, and z_{pg} variations may be neglected), allowing decoupling pyrolysis gas injection (material response) and boundary layer mass transport. For this presentation, we shall assume equal diffusion coefficients of the elements. Failure modes (spallation, mechanical erosion) are not included and the char is assumed to be composed of a single element (here : carbon).

The inputs and outputs to this problem are :

– Inputs : $\dot{m}_{pg}$, $z_{k,pg}$, $z_{k,ca} = 1$, $z_{k,e}$, p, T

– Outputs : $\dot{m}_{ca}$, $z_{k,w}$

The element fractions entering the control volume are computed by summing the convection and diffusion fluxes of elements. The conservation of the mass-fraction of element k in the control volume close to the wall reads :

$$j_{k,w} + (\rho V) z_{k,w} = \dot{m}_{pg} z_{k,pg} + \dot{m}_{ca} z_{k,ca} \tag{17}$$

where pg= pyrolysis gases, ca = char ablation products, w= wall (or control volume). The usual element-conservation rules apply :

– The relative mass fractions sum to 1 in each phase
$\sum_k z_{k,w} = 1$; $\sum_k z_{k,pg} = 1$; $\sum_k z_{k,ca} = 1$
– Since p, T are fixed, the element mass-fraction conservation in the control volume is equivalent to the mass conservation.

Under the hypotheses that Prandtl and Lewis numbers are equal to one and that the diffusion coefficients are equal for the elements, Eq. 17 may be rewritten as

$$\rho_e u_e C_H (z_{k,w} - z_{k,e}) + (\rho V) z_{k,w} = \dot{m}_{pg} z_{k,pg} + \dot{m}_{ca} z_{k,ca} \tag{18}$$

where, C_H is the Stanton number and $(\rho V) = \dot{m}_{pg} + \dot{m}_{ca}$.

The formation reaction of species A_i may be written :

$$A_i \rightleftharpoons \sum_{k \in Elements} \nu_{i,k} A_k \tag{19}$$

The i chemical equilibriums read :

$$\sum_{k \in Elements} \nu_{i,k} ln(x_k) - ln(x_i) - ln(K_i) = 0 \tag{20}$$

with $x_i = 1$ if A_i is a solid species. Species mole fractions sum to one :

$$\sum_{i \in Species} x_i = 1 \tag{21}$$

To sum up, the set of equations solved is (18, 20, and 21).

Once the new elemental composition in the control volume is obtained by solving the system above, the element fluxes at the surface of the material are computed, and used back as boundary conditions for the in-depth material model. Typically, for this type of simulations, mixed Dirichlet/Neumann

boundary conditions are used for total mass flow. When the flow goes inside the material (inflow), the element mass-fraction values are imposed at the boundary (Dirichlet), and when the flow goes outwards (outflow) a zero-gradient boundary condition is used (Neumann). In the present case, the problem is slightly more complex as for some of the species, the net transport (sum of convection and diffusion) might be directed inwards, while for other the net transport might be directed outwards. Therefore, to preserve total mass and improve convergence, the net fluxes are precomputed for each element, and the mixed Dirichlet/Neumann boundary condition is applied for each element.

3. Analysis of boundary-layer and pyrolysis gas flows within a porous Iso-Q sample

The model presented above has been implemented in the Porous material Analysis Toolbox based on OpenFoam (PATO) [20]. The MUlticomponent Transport And Thermodynamic properties/chemistry for IONized gases (Mutation++) is used to compute all chemistry and transport data, and to solve the surface mass balance equation [30].

As explained in the introduction, the objective of this section is to analyze boundary layer and pyrolysis gas flows within IsoQ samples . We have three objectives : 1) compare simplified and advanced pyrolysis gas flow models, 2) estimate their effect when inferring thermal conductivity from IsoQ experimental results, 3) provide a comprehensive understanding of boundary-layer gas flow within IsoQ samples.

As a reference case for this study, we will use case 3.1 of the 3rd ablation test-case series. It is a community-defined test-case, for which all material, geometry, and test-condition data are freely available. The ablation test-case series is an open forum to discuss modeling questions and compare simulation codes. The 3rd test-case series has been presented at the 6th ablation workshop [31]. It consists of an Iso-Q sample submitted to an arc-jet heat flux. The geometry of the sample is shown in Fig. 4. The geometry definition and thermocouple locations (Table 2) are inspired from a state-of-the-art arc-jet test already modeled using state-of-the-art codes [17, 32]. The sample geometry has been slightly modified from the usual sphere-cylinder geometry to an almost perfectly iso-flux ellipse-cylinder geometry displayed in Fig. 4. The heat load and test pressure have been chosen to bring the analysis in a regime relevant to flight. The specimen is subjected to a convective

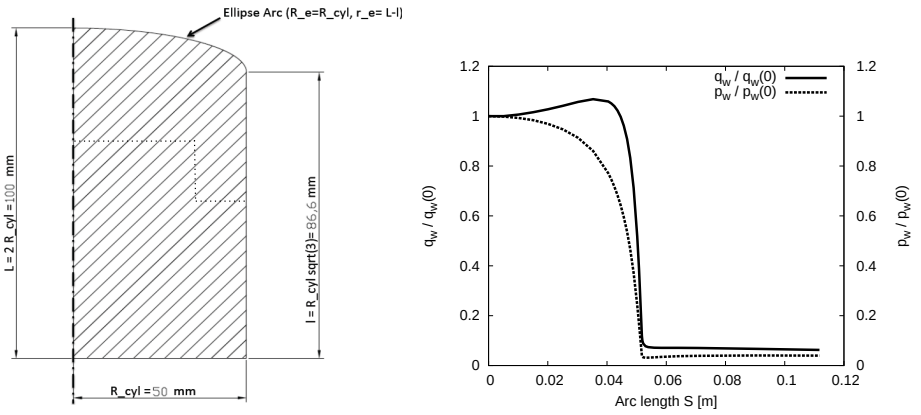

FIGURE 4: Iso-Q ellipse geometry, and pressure and temperature profiles provided in the 3rd ablation test-case series [31].

boundary condition (as described in subsection 2.2), with a test pressure of 0.1 atm and a heat flux of 2.5 MW/m^2 at the stagnation point. The sample is heated for 40 seconds, and it is let to cool-down for 1 minute by radiative cooling. The boundary conditions at the stagnation point are recalled in Table 1. The evolution of temperature, pressure, and solid density are studied at the locations provided in Table 2 and shown on Fig. 5.

The material of the case is the Theoretical Ablative Composite for Open Testing (TACOT), which is a low-density carbon/phenolic ablator [33, 34]. The properties of TACOT are open and available [31]. In volume, TACOT is made of 10% of carbon fibers, 10% of phenolic resin, and is 80% porous. Therefore its composition is comparable to NASA's Phenolic Impregnated Carbon Ablator [5, 6]. In this study, we will use the isotropic properties of PATO because we wish to keep the focus on the analysis of physical effects. It is then better to keep material properties as simple as possible to allow for a comprehensive understanding. The multi-block mesh used in PATO is shown in Fig. 5. The grid convergence study has shown that a fairly refined mesh was needed at the shoulder (Fig. 5-b) to capture the strong gas flows occurring at this location. The number of cells on the stagnation point line in the top block is 100, with a mesh refinement close to the surface. In the rest of the study, the orange block will have TACOT properties. The yellow block will either have TACOT properties or will be modeled as a purely conductive substructure material. The high-fidelity model is solved in the

ablative material block ; the energy conservation equation is solved in the substructure block. The coupling at the interface is enforced in a single step by a semi-implicit resolution of the following system : heat flux conservation and equal temperatures.

We will compare results for 3 cases :

- case A : is a simplification of case 3.1 (case B), where the outer pressure profile is constant and equal to the stagnation point pressure. This case replicates very closely simulations done to infer the properties of the Phenolic Impregnated Carbon Ablator (PICA) [17, 32].
- case B : reference case, as described above.
- case C : addition of a substructure that is impermeable to the gas flow, which is typically the case in a real test, when an ablative material is glued to a substructure. The substructure thermal properties are kept the same as for TACOT, as we wish to focus the study on flow effects.

The production code Samcef Amaryllis is used for the purpose of code-to-code comparison with PATO for the reference case (case B). Amaryllis is a finite element solver for charring ablators. It is being used as a design code for reentry applications [19]. Amaryllis solves the conservations equations for gas density, solid mass, gas momentum, and total energy. Element conservation is not implemented in Amaryllis ; instead, it is assumed that the gas composition within the sample remains constant during the analysis. The gas composition is considered to be pure pyrolysis gases in chemical equilibrium.

TABLE 1: Summary of the environment properties. Linear interpolation is used during the 0.1s heating and cooling periods (linear ramping).

time (s)	$\rho_e u_e C_h(stagnation)$ (kg$\cdot$ m$^{-2}\cdot$ s^{-1})	h_e (J$\cdot$ kg^{-1})	$p_{stagnation}$ (Pa)
0	$0.1 \cdot 10^{-2}$	0	405.3
0.1	0.1	$2.5 \cdot 10^{7}$	10132.5
40	0.1	$2.5 \cdot 10^{7}$	10132.5
40.1	$0.1 \cdot 10^{-2}$	0	405.3
120	$0.1 \cdot 10^{-2}$	0	405.3

In Figure 6, the iso-contours of pressure and temperature are shown for the 3 cases. The internal pressure increases inside the sample due to pyrolysis-gas production (red zone). The resulting pressure gradient leads to a gas flow that separates into two streams : one going towards the upper surface, and

Table 2: Location of the probes.

TC	Y-coordinate [cm]	Z-coordinate [cm]	TC	Y-coordinate [cm]	Z-coordinate [cm]
1	0.00	0.381	6	0.00	2.286
2	0.00	0.762	7	2.540	2.286
3	0.00	1.143	8	3.810	2.286
4	0.00	1.524	9	4.445	2.286
5	0.00	3.048	10	4.445	3.048

one going towards the bottom of the sample and then to the shoulder of the sample. This gas flow is at its maximum just under the shoulder for all cases (see Fig. 7), creating a local cooling that can be seen on the temperature plots. In case A, the pressure over the outer surface of the sample is constant and equal to the stagnation point pressure. Results will be the closest to cases computed with codes where the pyrolysis gas direction is prescribed along the mesh-lines perpendicular to the surface [17]. In case B, the real pressure profile (provided in figure 4) is applied. The outer pressure gradient forces more gas to exit the sample on the side, under the shoulder, where the pressure gradient is maximal. In case C, the fact of adding the substructure blocks the gas flows downwards, and forces more gas to exit through the upper surface and at the shoulder.

The gas flow patterns have a clear effect on temperature evolutions within the sample. The temperature evolutions at the thermocouple locations are presented in Fig. 8 (case B), 9 (case A), and 10 (case C). Fig. 8 shows a comparison between PATO and Amaryllis for the reference case (case B). The agreement between the two codes is excellent. In the configuration studied, the assumption of Amaryllis that the internal gases are pure pyrolysis gases does not affect the temperature profiles. We have run case B with PATO under the same hypothesis and confirmed this result. This is explained in the next section where the evolution of the gas composition within the material is studied in detail.

Case B is then used as a reference to be compared with case A, which is a simplification, and case C, which includes the substructure effect. In case A, the surface temperature at the stagnation point is lower. This is due to a larger pyrolysis gas flow at the stagnation point (blockage). The temperature of the shoulder thermocouples is in turn lower for case B due to the stronger

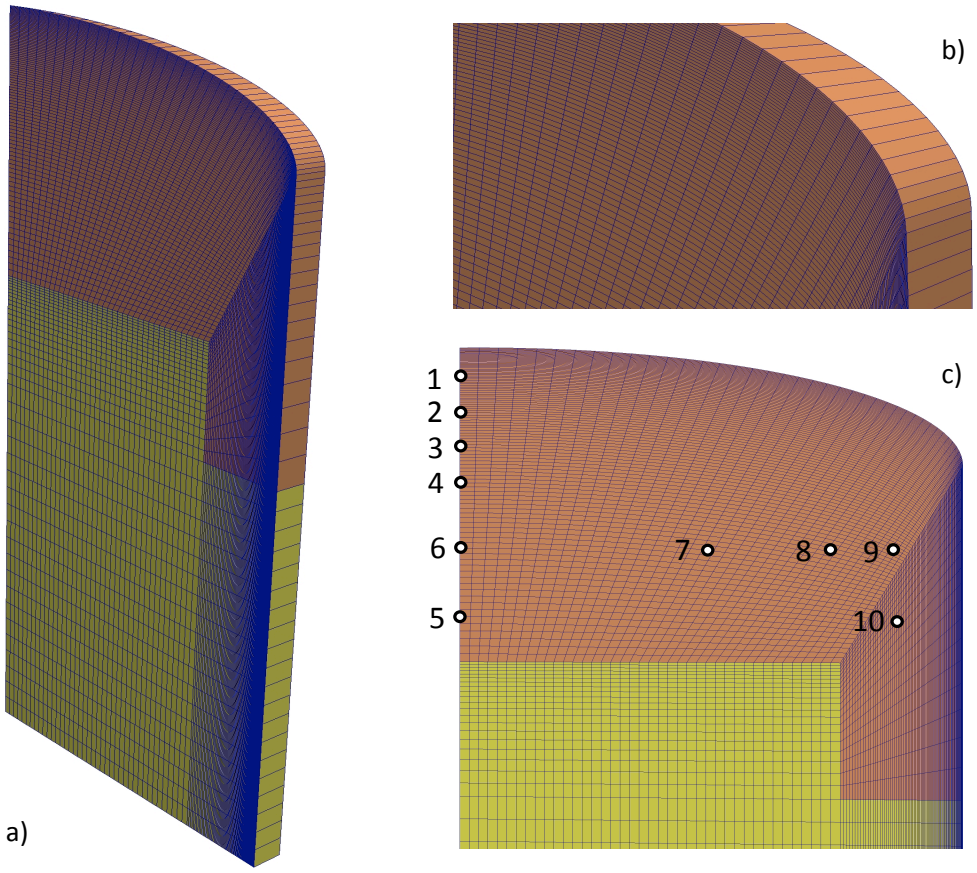

FIGURE 5: PATO multi-block mesh and thermocouple location. a) Wedge-mesh for axi-symmetrical simulations. 2) Zoom on the shoulder. 3) Thermocouple placement.

pyrolysis gas flow cooling down the shoulder. When comparing case C to case B, we see that all the internal thermocouples display a lower temperature. This is because less pyrolysis gas - which carries enthalpy - is convected downwards in case C. Instead, a larger amount of pyrolysis gases is directed towards the shoulder, reducing even more the shoulder temperature.

This theoretical analysis using fully open material properties and geometries shows some interesting perspectives for industrial applications. Indeed, when inferring equilibrium material response models, thermal conductivity is the most difficult parameter to determine in independent tests. Therefore, when finalizing a material model using IsoQ test-campaigns, the thermal

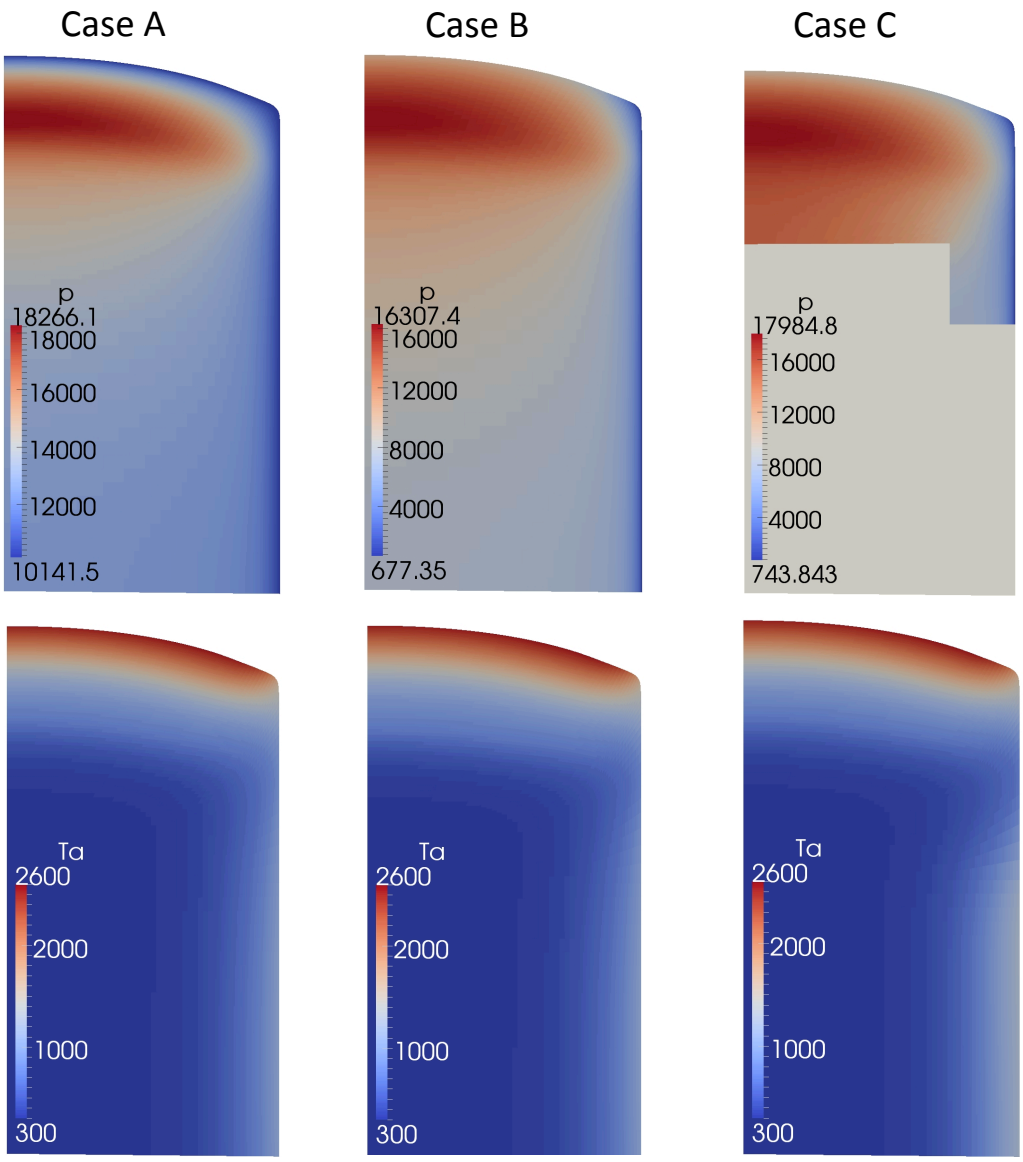

FIGURE 6: Pressure (in Pa) and temperature (in K) contours for cases A, B, and C at 40 seconds.

conductivity is generally fitted to match experimental data. We see here that this is a risky practice when using current state-of-the-art tools that do not model accurately the pyrolysis gas flow. For example, if the experimental

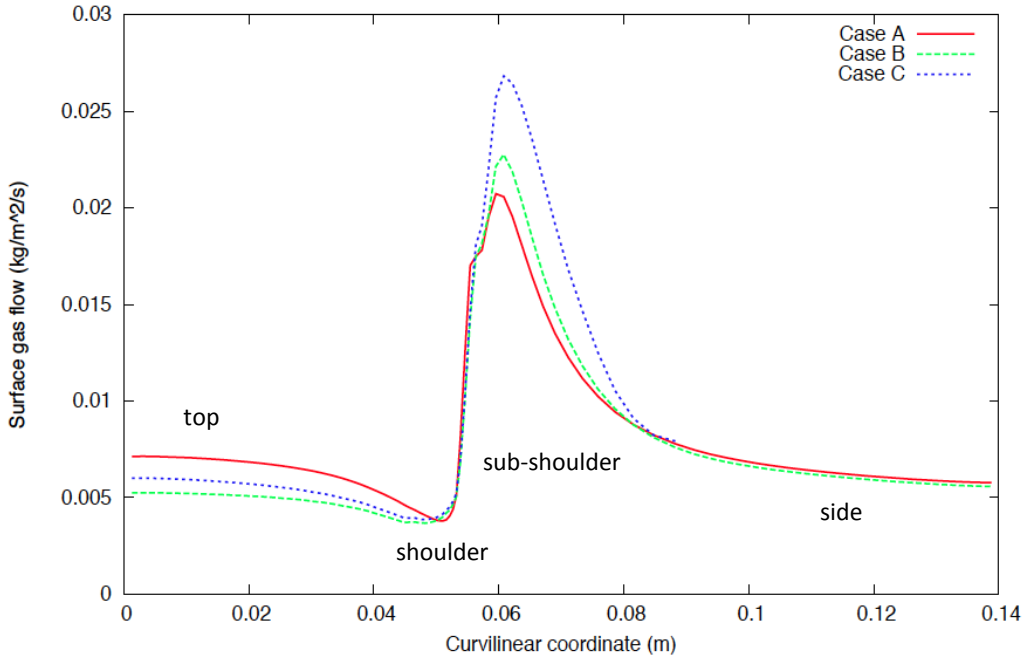

FIGURE 7: Comparison of the pyrolysis-gas flows at the surface of the sample ($\dot{m}_{pg}$) for cases A, B, and C at 10 seconds.

data were similar to the results of case C, and if we were using the model of case A, we would be tempted to add anisotropy properties to better match the thermocouple readings - to compensate for the lack of modeling of the pyrolysis gas flow. Once applied to other configurations, the optimized anisotropic dataset would then be inaccurate. It is very possible that porous material properties inferred from IsoQ experimental testing with simplified flow models [17] contain slightly incorrect conductivity values. The analysis of heritage IsoQ test data with the model and the tool of this study should enable a quantification of the uncertainties introduced in past analyses.

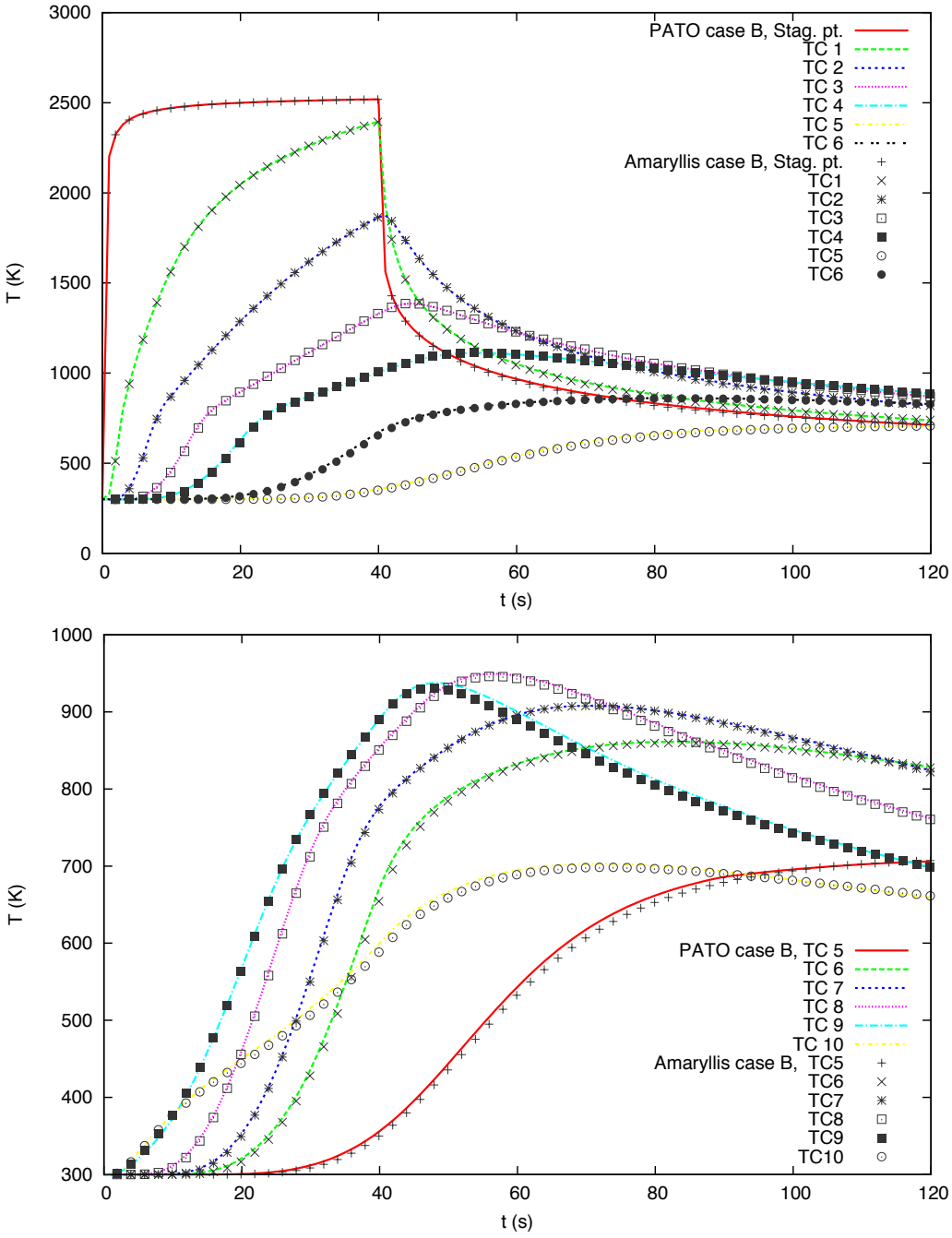

FIGURE 8: Temperature profiles : comparison of PATO and Amaryllis for case B (also Ablation Test-case 3.1) - reference solution.

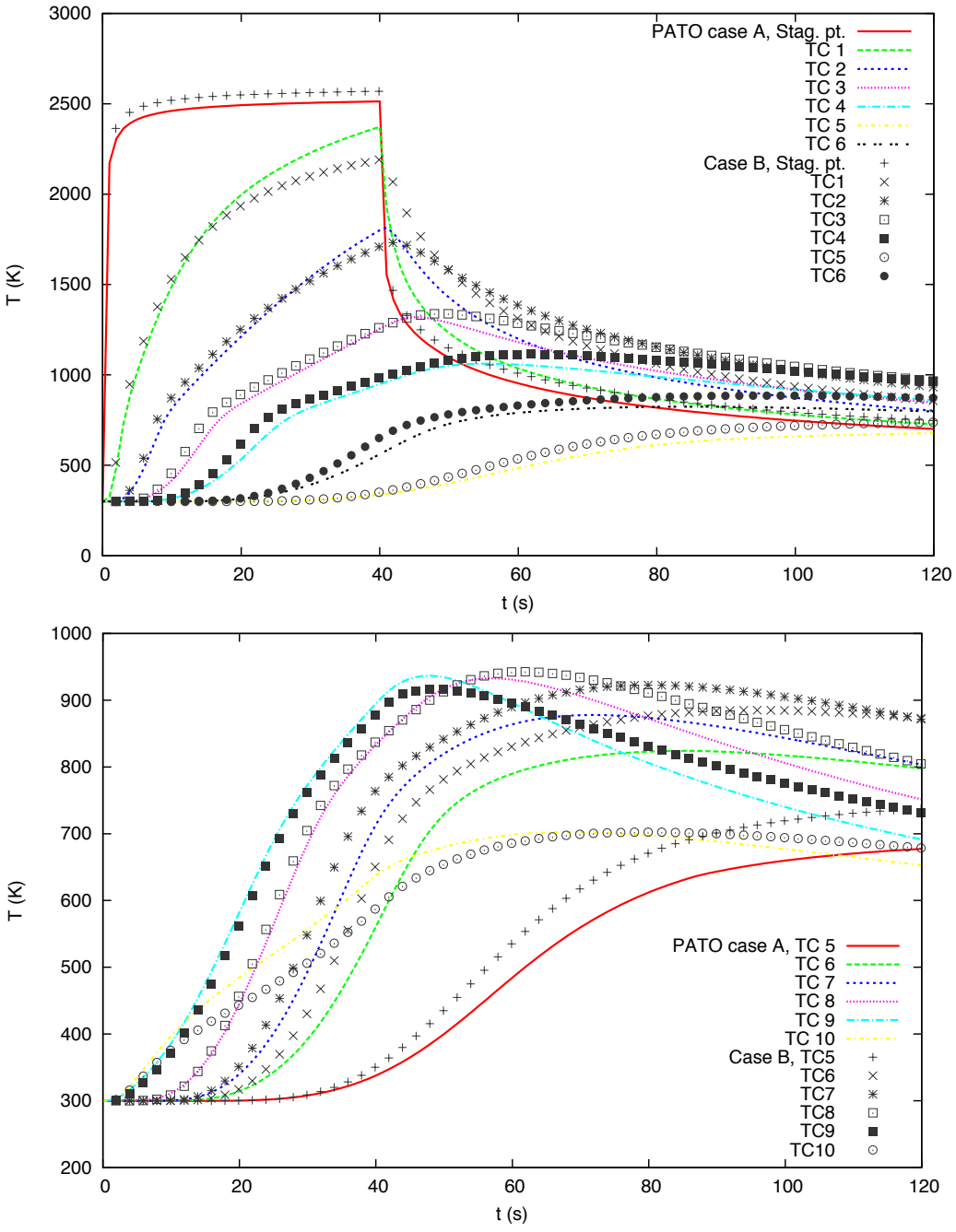

FIGURE 9: Temperature profiles : comparison of cases A and B.

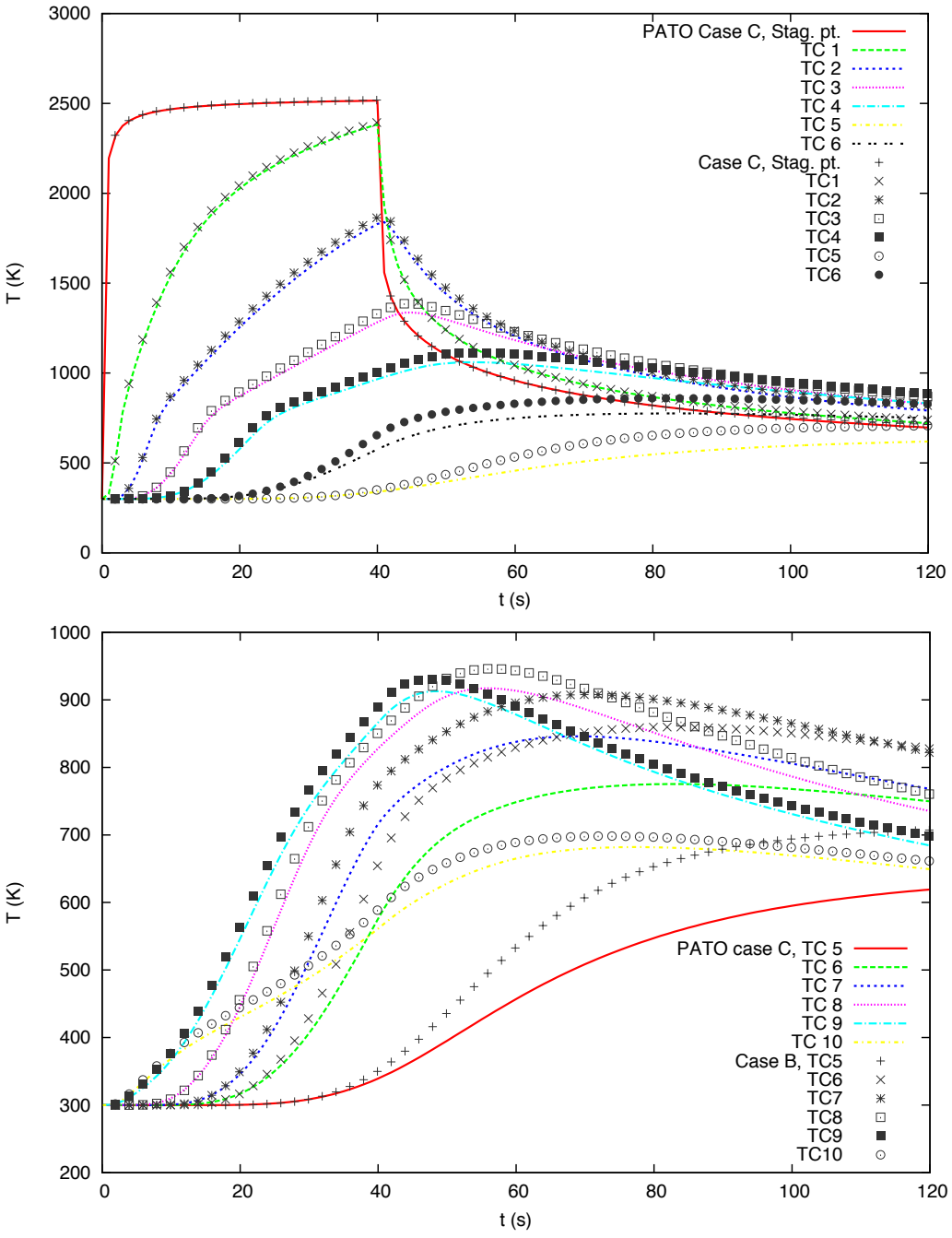

FIGURE 10: Temperature profiles : comparison of cases B and C.

3.1. Boundary layer gas flow

The simulation presented on Fig. 11 is based on case C. The detailed coupled-equilibrium model described in the modeling section is used. The simulation is initialized with pyrolysis gas within the porous material. This is the standard procedure for codes that do not track the elemental composition of the gas. When possible, it is of course better to start a simulation with the composition of the boundary layer gases. Here, we start on purpose with a different composition to clearly show the inflow of boundary layer gases, and we track the evolution of the elemental mass-fraction of nitrogen (N). At the start of the simulation, air enters into the sample, by convection at the top (due to the pressure gradient over the outer surface), and by diffusion on the side. Then, when the surface of the sample starts heating up, pyrolysis gases are produced. The internal pressure becomes higher than the external pressure and pyrolysis gases flow out at the upper face. They also build enough pressure to push back the internal gases to the bottom and to the side of the sample. Therefore, the boundary layer gases are blocked and they cannot percolate into the sample by the end of the ramping (0.1 s). Diffusion is still faster than convection on the side for 0.1 second. After 0.3 seconds, the pyrolysis gas production is sufficiently large to completely insulate the inside of the sample from the boundary layer gases. The composition of the gas within the sample is purely pyrolysis gas until the end of the simulation. With this transient being extremely short, the effect on the overall thermal response turns out to be negligible in the case of such simulations. Of course, we should be careful to not extend this conclusion to other configurations without verification.

4. Conclusion

A detailed model for porous composites under the equilibrium chemistry assumption within the material and in the boundary layer has been derived and implemented in the material response code PATO. The analysis of a theoretical case is presented to assess gas flow effects on material response. The case is based on the 3rd ablation test-case series. It consists in an Iso-Q sample submitted to a $2.5\,MW/m^2$ heat flux. The CFD-computed outer pressure and flux profiles are used as boundary conditions in the material code. The material of the study is the Theoretical Ablative Composite for Open Testing (TACOT), a low density porous carbon/phenolic ablator. The

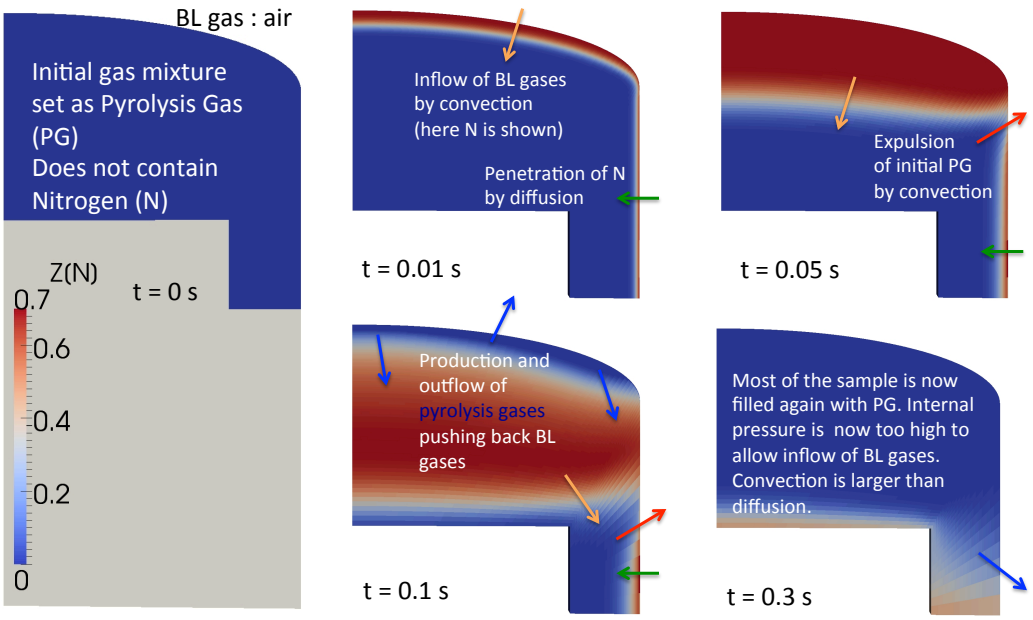

FIGURE 11: Inflow and outflow of boundary layer gases (in mass fractions) happening at the beginning of the simulation for case C.

internal pressure increases inside the sample due to pyrolysis-gas production. The resulting pressure gradient leads to a gas flow that separates into two streams : one going towards the upper surface, and one going towards the bottom of the sample, and then to the side towards the shoulder of the sample. This gas flow is at its maximum just under the shoulder creating a local cooling that can be seen on the temperature plots. Interestingly, boundary layer gases are rapidly blocked by outgasing pyrolysis products, even in the presence of a significant pressure gradient over the sample. Therefore, in the configuration studied, there is no urge to model boundary layer gas flow within the sample. We have studied several cases and configurations, and came to the conclusion that it is critical to model as accurately as possible pyrolysis-gas flow to obtain a correct temperature prediction, both in-depth and at the surface. According to this study, it is very possible that porous material properties inferred from IsoQ experimental testing with simplified flow models contain incorrect conductivity values. Therefore, it may be good to reassess them with the model proposed in this study.

Acknowledgments

Research of J.L. was originally funded by NASA's Fundamental Aeronautic Program Hypersonics NRA grant NNX12AG47A, it is currently supported by the Space Technology Research Grants Program. Research of T. E. M. is sponsored by the European Research Council Starting Grant #259354.

Bibliography

[1] J. D. Anderson, Hypersonic and high temperature gas dynamics, Mac Graw-Hill, New-York, 1989.

[2] G. Duffa, Ablative Thermal Protection Systems Modeling, AIAA, 2013, doi : 10.2514/4.101717.

[3] G. Savage, Carbon/Carbon composites, Chapman & Hall, London, 1993.

[4] T. Suzuki, K. Fujita, T. Yamada, Y. Inatani, N. Ishii, Postflight thermal protection system analysis of hayabusa reentry capsule, Journal of Spacecraft and Rockets 51 (1) (2014) 96–105, doi : 10.2514/1.A32549.

[5] H. K. Tran, C. E. Johnson, D. J. Rasky, F. C. L. Hui, M.-T. Hsu, T. Chen, Y. K. Chen, D. Paragas, L. Kobayashi, Phenolic impregnated carbon ablators (pica) as thermal protection systems for discovery missions, Tech. Rep. 110440, NASA Technical Memorandum (1997).

[6] M. Stackpoole, S. Sepka, I. Cozmuta, D. Kontinos, Post-flight evaluation of stardust sample return capsule forebody heatshield material.

[7] M. J. Wright, R. Beck, K. Edquist, D. Driver, S. Sepka, E. Slimko, W. Willcockson, T. DeCaro, H. Hwang, Sizing and margins assessment of the Mars Science Laboratory aeroshell thermal protection system, AIAA paper 2009-4231, 2009.

[8] K. T. Edquist, B. R. Hollis, C. O. Johnston, D. Bose, T. R. White, M. Mahzari, Mars science laboratory heat shield aerothermodynamics : Design and reconstruction, Journal of Spacecraft and Rockets 51 (4) (2014) 1106–1124, doi : 10.2514/1.A32749.

[9] H. Ritter, P. Portela, K. Keller, J. M. Bouilly, S. Burnage, Development of a european ablative material for heatshields of sample return missions, 6th European Workshop on TPS and Hot structures, Stuttgart, Germany, 1-3 April 2009.

[10] J. Lachaud, I. Cozmuta, N. N. Mansour, Multiscale approach to ablation modeling of phenolic impregnated carbon ablators, Journal of Spacecraft and Rockets 47 (6) (2010) 910–921.

[11] W.-S. Lin, Quasi-steady solutions for the ablation of charring materials, International Journal of Heat and Mass Transfer 50 (2007) 1196–1201.

[12] G. Duffa, G. L. Vignoles, J.-M. Goyheneche, Y. Aspa, Ablation of C/C composites : Investigation of roughness set-up from heterogeneous reactions, International Journal of Heat and Mass Transfer 48 (16) (2005) 3387–3401, doi :10.1016/j.ijheatmasstransfer.2005.02.036.

[13] J. Lachaud, Y. Aspa, G. L. Vignoles, Analytical modeling of the steady state ablation of a 3D C/C composite, International Journal of Heat and Mass Transfer 51 (9–10) (2008) 2614–2627, doi :10.1016/j.ijheatmasstransfer.2008.01.008.

[14] J. Lachaud, T. Magin, I. Cozmuta, N. N. Mansour, A short review of ablative material response models and simulation tools, in : E. S. Agency (Ed.), 7th Aerothermodynamics Symposium, Noordwijk, The Netherlands, 2011, pp 1-8.

[15] C. B. Moyer, R. A. Rindal, An analysis of the coupled chemically reacting boundary layer and charring ablator : Part II, NASA CR 1061, 168 p.

[16] M. A. Covington., J. M. Heinemann, Y.-K. Chen, I. Terrazas-Salinas, J. A. Balboni, J. Olejniczak, E. R. Martinez, Performance of a low density ablative heat shield material, Journal of Spacecrafts and Rockets 45 (4) (2008) 856–864.

[17] F. Milos, Y.-K. Chen, Ablation and thermal response property model validation for phenolic impregnated carbon ablator, Journal of Spacecrafts and Rockets 47 (5) (2010) 786–805.

[18] H. Weng, S. C. Bailey, A. Martin, Numerical study of iso-q sample geometric effects on charring ablative materials, Journal of Thermophysics and Heat Transfer 80 (1) (2015) 570–596, doi :10.1016/j.ijheatmasstransfer.2014.09.040.

[19] T. van Eekelen, J.-M. Bouilly, S. Hudrisier, J.-M. Dupillier, Y. Aspa, Design and numerical modelling of charring material ablators for re-entry applications, in : Proceedings of the Sixth European Workshop on Thermal Protection Systems and Hot Structures, European Space Agency - WPP-319, University Stuttgart, Germany, 2009.

[20] J. Lachaud, N. N. Mansour, Porous material analysis toolbox based on openfoam and applications, Journal of Thermophysics and Heat Transfer 28 (2) (2014) 191–202.

[21] S. Whitaker, The method of volume averaging, Kluwer Academic Publisher, Dordrecht, The Netherlands, 1999.

[22] H. W. Goldstein, Pyrolysis kinetics of nylon 6-6, phenolic resin, and their composites, Journal of macromolecular science, Part A 3 (4) (1969) 649–673.

[23] H. J. Ene, E. Sanchez-Palencia, On thermal equation for flow in porous media, International Journal of Engineering Science 20 (5) (1982) 623–630.

[24] N. Puiroux, M. Prat, M. Quintard, Non-equilibrium theories for macroscale heat transfer : ablative composite layer system, International Journal of Thermal Sciences 43 (6) (2004) 541–554.

[25] R. M. Kendall, E. P. Bartlett, R. A. Rindal, C. B. Moyer, An analysis of the coupled chemically reacting boundary layer and charring ablator : Part I, NASA CR 1060, 96 p.

[26] G. L. Vignoles, F. Langlais, C. Descamp, A. Mouchon, A. Mouchon, H. L. Poche, N. Reuge, N. Bertrand, CVD and CVI of pyrocarbon from various precursors, Surface and Coatings Technology 188–189 (2004) 241–249.

[27] J. Lachaud, N. Bertrand, G. L. Vignoles, G. Bourget, F. Rebillat, P. Weisbecker, A theoretical/experimental approach to the intrinsic oxidation reactivities of C/C composites and of their components, Carbon 45 (14) (2007) 2768–2776, doi :10.1016/j.carbon.2007.09.034.

[28] Y. K. Chen, F. S. Milos, Ablation and thermal response program for spacecraft heatshield analysis, Journal of Spacecraft and Rockets 36 (3) (1999) 475–483.

[29] C. B. Moyer, M. R. Wool, Aerotherm equilibrium surface thermochemistry computer program - version 3, Tech. rep., Aerotherm, aD875385 (April 1970).

[30] J. Scoggins, T. Magin, Development of Mutation++ : Multicomponent thermodynamic and transport property library for ionized plasmas written in c++, AIAA paper 2014-2966, 2014.

[31] T. van Eekelen, A. Martin, J. Lachaud, D. Bianchi, Ablation test-case series #3, version 2.0, Feb, 2013, 19 p.; prepared for the 6th Ablation Workshop, April 10-11 2014, University of Illinois at Urbana-Champaign. Retrieve : May 20, 2014 : http ://ablation2014.engineering.uky.edu/code-comparison/.

[32] J. A. Dec, R. D. Braun, B. Laub, Ablative thermal response analysis using the finite element method, Journal of Thermophysics and Heat Transfer 26 (2012) 201–212.

[33] J. Lachaud, A. Martin, I. Cozmuta, B. Laub, Ablation workshop test case - version 1.1 - feb. 2, 2011, prepared for the 4th Ablation Workshop (1-3 March 2011, Albuquerque, New Mexico).

[34] J. Lachaud, A. Martin, T. van Eekelen, I. Cozmuta, Ablation test-case series #2, version 2.8, Jan. 2011, 8 p., prepared for the 5th Ablation Workshop, Feb. 28-March. 1, Lexington, Kentucky.